INTERNATIONAL JOURNAL FOR NUMERICAL METHODS IN FLUIDS, VOL. 19, 647–665 (1994)

PREDICTION OF THERMAL STRATIFICATION IN A CURVED DUCT WITH 3D BODY-FITTED CO-ORDINATES

S. USHIJIMA

Central Research Institute of Electric Power Industry (CRIEPI), 1646 Abiko, Abiko-shi, Chiba-ken 270-11, Japan

SUMMARY

This paper concerns a numerical prediction method for buoyancy-influenced flows using three-dimensional non-orthogonal curvilinear co-ordinates. The numerical analysis of the transformed governing equations for thermal hydraulics is based on a Lagrangian method, in which advected physical values are evaluated by local cubic spline interpolations with third-order accuracy in the three-dimensional computational domain. In addition, the buoyancy and diffusion terms are discretized in the Lagrangian scheme so as to have second-order accuracy with respect to time and space. The Neumann boundary conditions, which have been rather difficult for non-orthogonal co-ordinates to deal with, can be implemented by making use of normal vectors on the physical boundary surfaces and cubic spline interpolations. The developed numerical method is applied to the steady isothermal flow in a curved pipe and the unsteady stratified flow in a curved duct. Both of the predicted values are in good agreement with the experimental results and the validity of the prediction method is confirmed.

KEY WORDS Curvilinear co-ordinate Lagrangian method Spline interpolation Neumann condition Thermal stratification

1. INTRODUCTION

It is of great necessity to predict accurately thermally stratified flows occurring in engineering facilities, such as coolant piping systems in a nuclear reactor, since the stratified flows may bring about thermal effects on structures which lead to thermal fatigue damage. In many practical problems, however, the buoyancy-influenced flows are usually surrounded by complicated-shaped boundaries, which makes it difficult to apply numerical methods based on Cartesian co-ordinates.

In order to represent these arbitrarily shaped boundaries, numerical techniques utilizing body-fitted curvilinear co-ordinates have been developed up to the present. Among these numerical techniques, one of the most advantageous methods is to obtain the body-fitted co-ordinates by solving a system of elliptic partial differential equations in which the co-ordinates in physical space are converted to be dependent variables.[1] This numerical technique was initially applied by Winslow,[2] Barfield[3] Chu[4] and Amsden and Hirt.[5] Thompson *et al.*[6–8] then largely developed the elliptic method by extending it to multiply connected regions and by adding control functions to the Laplace equations in order to adjust the grid intervals.

When taking the transformed co-ordinates to be the solutions of the Poisson equation, a non-orthogonal curvilinear co-ordinate system is available. The non-orthogonal curvilinear co-ordinates utilized in the present study are generated with the aid of cubic spline interpolations as done by Hsu and Lee.[9] As a result, the derived metric coefficients contain truncation errors

CCC 0271–2091/94/200647–19

Received 27 July 1993
Revised 12 January 1994

smaller than those raised by the central difference method employed in previous investigations.[10–12] In addition, the physical quantity at the intersection of the normal vector on the physical boundary surface and the curvature in the vicinity of the boundary is made use of in order to deal with Neumann boundary conditions in the present numerical method.

The accurate numerical analysis of the governing equations for thermal hydraulics is necessary especially when the transformed equations are discretized and solved in the computational domain. In particular, the discretization of convection terms must be paid attention in order to obtain reliable numerical results. While second-order upwind difference and central difference were sometimes employed in the past,[10,12] their numerical accuracy or computational stability is not necessarily satisfactory. Similar aspects may also be pointed out with the quadratic interpolation method. While Ogawa and Ishiguro[13] applied a third-order upwind scheme,[14] there have been few calculations conducted with third-order accuracy in the transformed space. In contrast with the usual numerical techniques, the equation of motion and the energy equation are discretized in the transformed space with a Lagrangian method in the present study. Lagrangian schemes for convection phenomena are capable of providing satisfactory accuracy as indicated by Holly and Preissmann[15] and Schohl and Holly.[16] These Lagrangian interpolations were, however, applied to a fairly simple geometry and require a large amount of computational time in a three-dimensional domain consisting of many calculation grids. In order to achieve highly accurate interpolation within a reasonable computational time, local cubic spline interpolation, which provides more reliable results than third-order upwind difference, is proposed to evaluate convection terms in the present study. In addition, the discretization of the buoyancy and diffusion terms, which has not fully been investigated in Lagrangian schemes, is performed so that they can have second-order accuracy with respect to time and space.

The developed prediction method is applied to the steady isothermal flow in a curved pipe[17] and the unsteady thermally stratified flow arising in a curved duct. As a result, the predicted axial velocity distributions and secondary flow patterns in the pipe agree well with the measured results. In addition, the progress of thermal stratification, vertical temperature profiles and other experimentally observed aspects are reasonably predicted in the curved duct.

2. NUMERICAL PROCEDURE

Generation of body-fitted co-ordinates

Let (x_1, x_2, x_3) be a Cartesian co-ordinate system defined in the three-dimensional physical space. The non-orthogonal curvilinear co-ordinate system (ξ_1, ξ_2, ξ_3) is obtained as the solution of the Poisson equation

$$\frac{\partial^2 \xi_m}{\partial x_i \partial x_i} = P_m, \tag{1}$$

where the Einstein summation rule is applied to the terms bearing the same subscripts twice. The co-ordinates (ξ_1, ξ_2, ξ_3), fitted to the arbitrarily shaped boundaries in the physical space, make up a regular orthogonal co-ordinate system in the computational (or transformed) domain. The control functions P_m in equation (1) are given as exponential forms, which adjust the grid intervals as proposed by Thompson *et al.*[7] Equation (1) may be inversely transformed by interchanging the dependent and independent variables as

$$\left(\frac{\partial^2 x_i}{\partial \xi_p \partial \xi_q}\right)^* \left(\frac{\partial \xi_p}{\partial x_j}\right)^* \left(\frac{\partial \xi_q}{\partial x_j}\right)^* + \frac{\partial^2 x_i}{\partial \xi_r \partial \xi_s} \left(\frac{\partial \xi_r}{\partial x_j}\right)^* \left(\frac{\partial \xi_s}{\partial x_j}\right)^* + P_m \left(\frac{\partial x_i}{\partial \xi_m}\right)^* = 0, \tag{2}$$

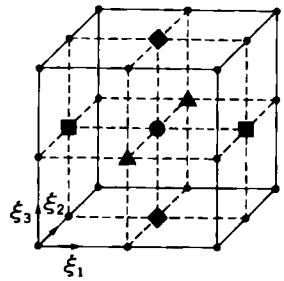

Figure 1. Unit computational volume in transformed space (●, scalar value; ■, U_1; ▲, U_2; ◆, U_3)

where $p \neq q$ and $r = s$. Here the derivatives with an asterisk are evaluated not by the usual central difference but from cubic spline interpolation. This interpolation is referred to as general cubic spline interpolation (GCSI) in the present paper, in which a cubic spline function is determined in order that its first and second derivatives should be continuous in a whole computational region. In particular, the cross-derivatives in the first term of equation (2) are calculated by applying GCSI again to the first derivatives obtained by GCSI. Consequently, only the second derivatives in the second term of equation (2) are discretized with the central difference and the derived finite difference equations are solved by a successive overrelaxation method. Since GCSI allows us to calculate the derivatives with an accuracy higher than the central difference, the metric coefficients are finally evaluated with less truncation error compared with the usual methods.

A unit computational volume in the transformed space consists of 27 grids as shown in Figure 1 and all their locations in the physical space are determined by solving equation (2). The pressure and temperature variables are placed at the centre grid in the unit volume, while each contravariant velocity component is defined at the centre grid on the surface normal to its direction. In contrast with such a staggered arrangement inside the computational domain, the grid arrangements are varied near the boundaries and the physical quantities are defined just on the transformed boundary planes so that Dirichlet boundary conditions can be implemented exactly. When a certain physical value at a grid point needs to be evaluated at another grid located in a different position, it is interpolated with GCSI in the computational domain rather than simple linear interpolation.

Equation of motion

The equation of motion with the Boussinesq approximation may be written in the following form in the computational domain:

$$\frac{\mathrm{D}u_i}{\mathrm{D}t} = -\frac{1}{\rho_S}\frac{\partial p}{\partial \xi_m}\frac{\partial \xi_m}{\partial x_i} + \frac{\Delta\rho}{\rho_S}F_i + \nu_S\left(\frac{\partial^2 u_i}{\partial \xi_m \partial \xi_n}\frac{\partial \xi_m}{\partial x_j}\frac{\partial \xi_n}{\partial x_j} + P_m\frac{\partial u_i}{\partial \xi_m}\right). \tag{3}$$

Here $\mathrm{D}/\mathrm{D}t$ denotes Lagrange differentiation in the transformed space, given by $\mathrm{D}/\mathrm{D}t = \partial/\partial t + U_m\partial/\partial\xi_m$, where the contravariant velocity component U_m is defined by $U_m = u_i\partial\xi_m/\partial x_i$. The pressure p corresponds to the deviation from that of the hydrostatic condition. The second term on the right-hand side of equation (3) represents the effect of buoyancy force, where $\Delta\rho$ may be approximated by a linear relationship as $\Delta\rho = -\beta(T - T_S)$. Let the pressure gradient,

buoyancy and diffusion terms on the right-hand side of equation (3) be PG_i, B_i and D_i respectively. Then equation (3) can be rewritten in the simple form

$$\frac{\mathrm{D}u_i}{\mathrm{D}t} = -PG_i + B_i + D_i \equiv FU_i. \tag{4}$$

On the basis of Taylor expansion for total differentiation, $u_i(t, \xi_1, \xi_2, \xi_3)$ can be expressed by $u_i(t - \Delta t, \xi_1 - \Delta\xi_1, \xi_2 - \Delta\xi_2, \xi_3 - \Delta\xi_3)$, which is defined at the earlier upstream point. Let the superscript n be the computational time step number, where $t = n\Delta t + t_0$, and let the superscript 'prime' stand for the spatial location at the upstream point P' $(\xi_1 - \Delta\xi_1, \xi_2 - \Delta\xi_2, \xi_3 - \Delta\xi_3)$. Now we may derive

$$u_i^{n+1} = u_i'^n + \mathrm{D}u_i'^n + \tfrac{1}{2}\mathrm{D}^2 u_i'^n + \Delta^3. \tag{5}$$

Here D denotes total differentiation with respect to time and space. From equation (4) the relationship $\mathrm{D}u_i'^n = FU_i'^n\Delta t$ may be derived, and substituting it into equation (5), we have

$$u_i^{n+1} = u_i'^n + FU_i'^n\Delta t + \tfrac{1}{2}\mathrm{D}(FU_i'^n)\Delta t + \Delta^3. \tag{6}$$

In addition, taking Taylor expansion for $FU_i''^{n-1}$ yields

$$FU_i''^{n-1} = FU_i'^n - \mathrm{D}FU_i'^n + \Delta^2. \tag{7}$$

Here the superscript 'double prime' stands for the spatial position at

$$\mathrm{P}''\,(\xi_1 - \Delta\xi_1 - \Delta\xi_1', \xi_2 - \Delta\xi_2 - \Delta\xi_2', \xi_3 - \Delta\xi_3 - \Delta\xi_3').$$

Applying equation (7) to equation (6), we can derive

$$u_i^{n+1} = u_i'^n + \tfrac{3}{2}FU_i'^n\Delta t - \tfrac{1}{2}FU_i''^{n-1}\Delta t + \Delta^3. \tag{8}$$

The upstream positions of P' and P'' may be specified by the following relationships: $\Delta\xi_m = U_m^n\Delta t$ and $\Delta\xi_m' = U_m'^{n-1}\Delta t$. The pressure gradient term included on the right-hand side of equation (8) is dealt with implicitly as

$$PG_i^{n+1} \equiv \tfrac{3}{2}PG_i'^n - \tfrac{1}{2}PG_i''^{n-1}. \tag{9}$$

Accordingly, equation (8) becomes

$$u_i^{n+1} = u_i'^n - PG_i^{n+1}\Delta t + [\tfrac{3}{2}(B_i'^n + D_i'^n) - \tfrac{1}{2}(B_i''^{n-1} + D_i''^{n-1})]\Delta t. \tag{10}$$

While the above discretization for buoyancy and diffusion terms looks like the Adams–Bashforth method[18] in terms of time differencing, it should be noted that the discretization extends to two spatial locations P' and P'' as well as two time steps, which results in the second-order accuracy of these terms with respect to time and space in Lagrangian schemes.

Local cubic spline interpolation

The physical values located at P' and P'' are derived with local cubic spline interpolation (LCSI) which utilizes the physical values included in a local three-dimensional domain consisting of N^3 grid points, in contrast with GCSI using all values in the computational region. LCSI

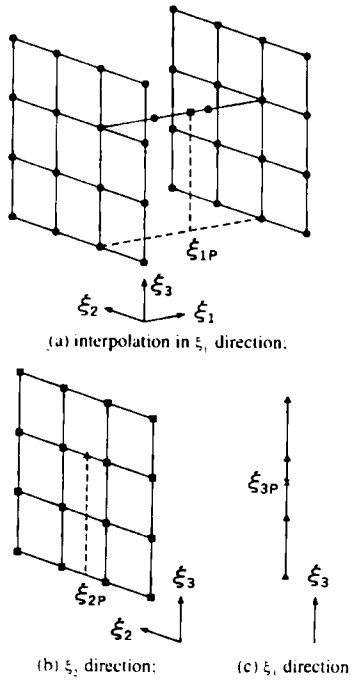

Figure 2. Local cubic spline interpolation

can reduce the computational time compared with GCSI, especially when the grid number in the computational region becomes large.

In the case where $N = 4$ and the location of P′ or P″ is given by $(\xi_{1P}, \xi_{2P}, \xi_{3P})$, one-dimensional cubic spline functions are determined from four physical values lined in the ξ_1-direction as shown in Figure 2(a). The 16 derived spline functions provide the 16 interpolated values at (ξ_{1P}, ξ_2, ξ_3). Then, as shown in Figure 2(b), four physical values are similarly interpolated at $(\xi_{1P}, \xi_{2P}, \xi_3)$ by cubic spline interpolation four times in the ξ_2-direction. Lastly, the physical value at P′ or P″ is determined by interpolation in the ξ_3-direction as indicated in Figure 2(c). In order to obtain the one-dimensional cubic spline function used in the above interpolation, the first derivatives of the physical values are necessary at both ends of the lined grids. These boundary conditions are determined from the polynomial of degree $N - 1$, which is uniquely derived with N physical values.

Calculation of pressure and velocity

Differentiating equation (10) with respect to x_i and putting the dilation at step $n + 1$ to zero as suggested by Harlow and Welch,[19] we can obtain the following equation for pressure:

$$\frac{1}{\rho_S}\left[\frac{\partial^2 p^{n+1}}{\partial\xi_m\partial\xi_n}\left(\frac{\partial\xi_m}{\partial x_j}\right)^*\left(\frac{\partial\xi_n}{\partial x_j}\right)^* + \mathrm{P}_m\frac{\partial p^{n+1}}{\partial\xi_m}\right]\Delta t$$
$$= \frac{\partial U_m''^n}{\partial\xi_m} + \frac{3}{2}\left(\frac{\partial\xi_m}{\partial x_i}\right)^*\left(\frac{\partial}{\partial\xi_m}(B_i'^n + D_i'^n)\Delta t\right)^* - \frac{1}{2}\left(\frac{\partial\xi_m}{\partial x_i}\right)^*\left(\frac{\partial}{\partial\xi_m}(B_i''^{n-1} + D_i''^{n-1})\Delta t\right)^*. \quad (11)$$

Here the terms with an asterisk are evaluated with GCSI, while the metric coefficients included in equation (11) have already been determined with GCSI in the generation of curvilinear co-ordinates.

The buoyancy and diffusion terms B_i and D_i respectively are first calculated at the grid points, where corresponding velocity components are defined, with the following forms:

$$B_i = -\frac{1}{\rho_S}\beta(T^* - T_S)F_i, \tag{12}$$

$$D_i = \nu_S\left[\left(\frac{\partial^2 u_i}{\partial\xi_m\partial\xi_n}\right)^*\left(\frac{\partial\xi_m}{\partial x_j}\right)^*\left(\frac{\partial\xi_n}{\partial x_j}\right)^* + P_m\left(\frac{\partial u_i}{\partial\xi_m}\right)^*\right]. \tag{13}$$

Here the temperature and first and second derivatives of velocity with an asterisk are evaluated with GCSI, referring to all values in the computational domain. The derived B_i and D_i at time steps n and $n-1$ are then interpolated at P′ and P″ respectively with the aid of LCSI. Finally, their derivatives with respect to ξ_m are calculated by applying GCSI to $B_i'^n + D_i'^n$ and $B_i''^{n-1} + D_i''^{n-1}$ and the corresponding terms in equation (11) are obtained.

The second derivative of pressure in equation (11) are discretized with central difference and the converged results are obtained from iterative calculations. In the vicinity of boundary surfaces, where the intervals of grid positions are changed, the pressure discretization in equation (11) is also conducted so as to have second-order accuracy by taking Taylor expansion up to third-order terms.

The results of the pressure calculation are substituted into the equation of motion given by (10), where pressure gradients are evaluated with GCSI. While the combination of equations (10) and (11) might not be the best way to derive the converged solutions for pressure in terms of its efficiency, the present numerical simulations descried later were carried out so that the average discrete dilation normalized by flow rate can be kept at less than 10^{-6} in the steady state, which can be thought as a sufficient level for the fluid continuity.

The convection term, the first term on the right-hand side of equation (10), is calculated with LCSI in which local 64 physical values are utilized in the interpolation ($N = 4$). Since the buoyancy and diffusion terms in equation (10) have already been obtained in the pressure calculation, these values are used again to solve equation (10).

Energy equation

The energy equation in the transformed space may be written as

$$\frac{DT}{Dt} = \alpha\left(\frac{\partial^2 T}{\partial\xi_m\partial\xi_n}\frac{\partial\xi_m}{\partial x_j}\frac{\partial\xi_n}{\partial x_j} + P_m\frac{\partial T}{\partial\xi_m}\right) \equiv FT. \tag{14}$$

The discretized equation can be derived with reference to the result of the momentum equation (10) as

$$T^{n+1} = T'^n + \tfrac{3}{2}FT'^n\Delta t - \tfrac{1}{2}FT''^{n-1}\Delta t. \tag{15}$$

The diffusion terms included in equation (15) are first calculated with the following equation at the gird point where temperature is defined:

$$FT = \alpha\left[\left(\frac{\partial^2 T}{\partial\xi_m\partial\xi_n}\right)^*\left(\frac{\partial\xi_m}{\partial x_j}\right)^*\left(\frac{\partial\xi_n}{\partial x_j}\right)^* + P_m\left(\frac{\partial T}{\partial\xi_m}\right)^*\right]. \tag{16}$$

Here the first and second derivatives of temperature with an asterisk are evaluated by GCSI using all values in the computational domain. Then the derived FT at steps n and $n-1$ are interpolated at P′ and P″ respectively by LCSI in order to obtain the second and third terms on the right-hand side of equation (15). The remaining convection term in equation (15) is evaluated with LCSI in a manner similar to the calculation of the convection term in equation (10).

Boundary conditions

Since the intervals of the grid points are varied near the boundary and they are placed just on the boundary surface, the Dirichlet conditions are readily incorporated by setting the appointed values at the grids existing on the boundary surfaces. In contrast, it has been noted that the Neumann conditions, such as thermally insulated conditions, are rather difficult for non-orthogonal curvilinear co-ordinates to deal with. To improve this aspect, the intersection of the normal line on the physical boundary surface and the curvature in the vicinity of the boundary is specified and then its physical value, which is needed to satisfy the Neumann conditions, is interpolated with GCSI.

Figures 3 and 4 illustrate how to implement the Neumann conditions on the ξ_1–ξ_2 boundary where $\xi_3 = 0$, for example. Once the tangential vectors $\mathbf{T}_1$ and $\mathbf{T}_2$ along ξ_1 and ξ_2 respectively are obtained at P_b on the boundary, the normal vector $\mathbf{n}$ on the surface is determined by

$$\mathbf{n} = \mathbf{T}_1 \times \mathbf{T}_2. \tag{17}$$

The normal vector $\mathbf{n}$ is transformed to $\mathbf{h}$ in the computational domain as

$$h_l = n_j \frac{\partial \xi_l}{\partial x_j}. \tag{18}$$

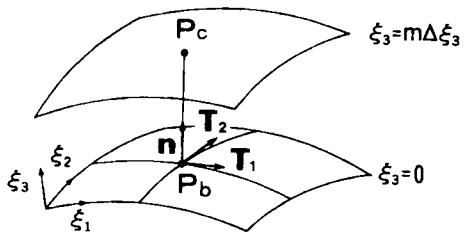

Figure 3. Normal and tangential vectors on physical boundary surface

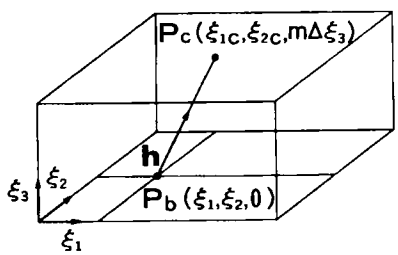

Figure 4. Normal vector on transformed boundary surface

When the intersection of the normal line and the curvature where $\xi_3 = m\Delta\xi_3$ is given by P_C in the physical space as indicated in Figure 3, the corresponding intersection in the transformed space may be specified as the point where the extension line of **h** crosses the $\xi_3 = m\Delta\xi_3$ plane. Once the location of the intersection is singled out in the computational domain, the physical value at P_C is easily evaluated with GCSI. In the present method, when physical values F_1 and F_2 are interpolated with GCSI in the $\xi_3 = m_1\Delta\xi_3$ and $m_2\Delta\xi_3$ planes respectively, the physical value on the boundary surface, F_b, is given by

$$F_b = \frac{1}{(2D_1 + D_2)D_2}\left((D_1 + D_2)^2F_1 - D_1^2F_2 - (D_1 + D_2)D_1D_2\frac{\partial F}{\partial n}\right), \tag{19}$$

where D_1 and D_2 are the distances between P_b and the intersections. From equation (19), when the gradient of F in the normal direction is provided as $\partial F/\partial n$, the Neumann boundary condition is determined with second-order accuracy.

3. RESULTS AND DISCUSSION

Pure advection computed by LCSI

With reference to the advection–diffusion equation given by (15), the pure advection of a scalar value C may be described in the Lagrangian method as

$$C^{n+1} = C'^{n}. \tag{20}$$

The accurate evaluation of the pure advection is necessary to obtain reliable computational results. Figure 5 shows the two-dimensional grid distribution in a circular area, where the predicted scalar profiles are compared among some different numerical methods. It is assumed that the constant velocity distributions ($u = v = U_C$) are given in the whole area and that the step-shaped scalar distribution is provided at the upstream section as illustrated in Figure 5. The purely advected scalar values are predicted with LCSI, third-order polynomial interpolation[20] (POL3D), third-order upwind difference[14] (UPW3D) and usual first-order upwind difference (UPW1D). The filtering remedy and methodology[21] (FRAM) is applied to LCSI and

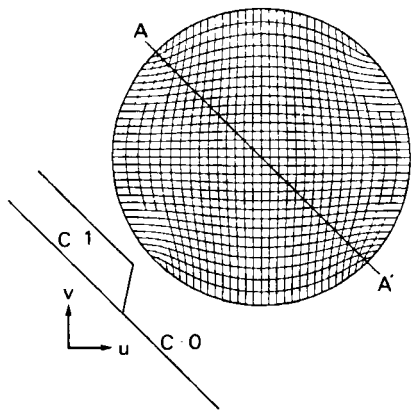

Figure 5. Calculation area and scalar boundary condition

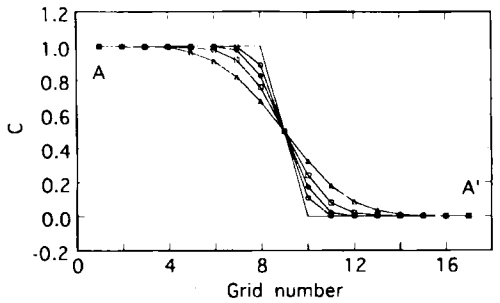

Figure 6. Comparison of scalar profiles (—, theory; ○, LCSI; ◇, POL3D; □, UPW3D; △, UPW1D)

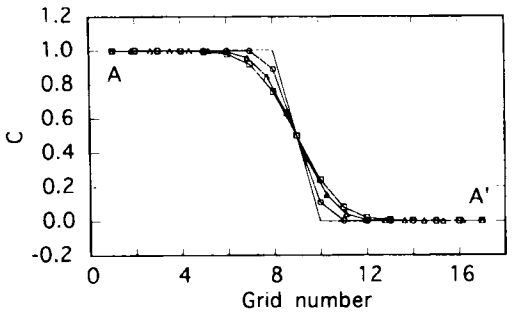

Figure 7. Comparison of scalar profiles (—, theory; ○, LCSI; △, UPW3DF; □, UPW3D)

POL3D to prevent unphysical oscillation. The computational time step is fixed at $0{\cdot}01D_C/U_C$ in all cases, where D_C is the diameter of the calculation area. Figure 6 shows the predicted scalar profiles across section A–A′ indicated in Figure 5. It is obvious that LCSI offers the most reliable scalar distribution in the predicted results shown in Figure 6.

Regarding the computational efficiency, LCSI needed about seven times longer computational time than UPW3D in this pure advection problem. However, when they are applied to the fluid calculation in the curved duct as described later, which includes pressure calculation and all the other numerical procedures, it has been confirmed that LCSI requires only 1·5 times longer computational time than UPW3D. Figure 7 shows the predicted scalar distribution using third-order upwind difference on the finer grid distribution (UPW3DF). This UPW3DF is expected to require almost the same computational time as LCSI on the relatively coarse grid arrangement when they are applied to the calculation of the flow in the curved duct. In Figure 7, although UPW3DF offers slightly improved results compared with UPW3D owing to the finer mesh arrangement, the scalar distribution obtained by LCSI is still much better than that of UPW3DF. This means that LCSI is superior to third-order upwind difference even if the computational time and the required computer memory are taken into account. In addition, with regard to the effect of the Courant number on LCSI, no significant differences were found in the range from the average Courant number 0·07 to 0·4 in this pure advection problem.

Steady isothermal flow in a curved pipe

Detailed velocity measurements for the steady entry flow in a pipe with a 90° bend, which has a Reynolds number of 700, were carried out by Bovendeerd *et al.*[17] This flow is numerically

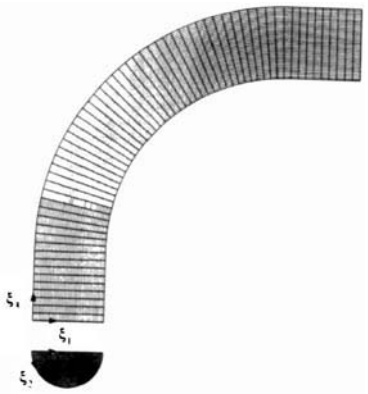

Figure 8. Computational grids for curved pipe

simulated with the present method under the same hydraulics conditions as their experiment. The pipe has an internal radius of 4·0 mm and a radius of curvature of 24·0 mm, which is represented in the numerical simulation as a pipe with a half-circular cross-section owing to the symmetry of the flow observed in the experiment. Figure 8 shows the distribution of the computational grids generated by solving equation (2). The total grid number is $\xi_1 \times \xi_2 \times \xi_3 = 35 \times 21 \times 63 = 46{,}305$ and the number of grids where pressure is defined is $19 \times 12 \times 33 = 7524$. The incoming velocity is given as a parabolic distribution on the inlet section, which is located one diameter (8·0 mm) upstream from the entrance of the bend, taking into account that a fully developed flow was observed at the entrance in the experiment.

Figure 9 shows the calculated velocity vectors on the section of symmetry. The development of the predicted axial flow is compared with the experimental results in Figure 10. The angles of the sections shown in Figure 10 are defined with respect to the entrance section of the bend. The parabolic velocity distribution is almost maintained up to $\theta = 11{\cdot}7°$ and the visible shift of the point of maximum axial velocity towards the outer bend is observed at $\theta = 23{\cdot}4°$ for the first time. The maximum of axial velocity still shifts towards the outer bend on the further downstream sections. On the other hand, a low axial velocity region develops near the inner

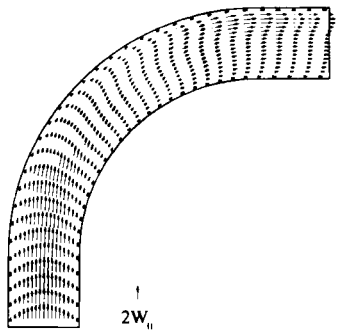

Figure 9. Calculated velocity vectors on section of symmetry

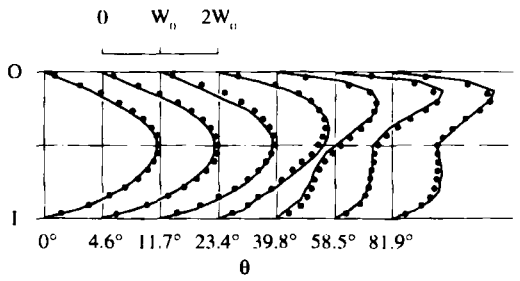

Figure 10. Development of axial flow (—, experimental results obtained by Bovendeerd *et al.*[17]; ●, predicted results; O, outer bend; I, inner bend)

bend. In Figure 10 it can be seen that the predicted axial velocity distributions are generally in good agreement with the experimental values.

Figure 11 shows the development of the secondary flow. At the first section most of the predicted velocity vectors are directed towards the inner wall. At $\theta = 4{\cdot}6°$ a weak clockwise circulation arises in the section and near the symmetry plane the flow is directed from the inner to the outer bend. The vortex has intensified on the following sections ($\theta = 11{\cdot}7°$ and $23{\cdot}4°$) and the predicted secondary flow patterns are almost symmetric with respect to the vertical centreline. On the following sections ($\theta = 39{\cdot}8°$ and $58{\cdot}5°$) the predicted vortex centre has moved to the inner wall and the vortex intensity has gradually decreased. At the last section ($\theta = 81{\cdot}9°$) the predicted vortex has developed a 'tail' as observed by Bovendeerd *et al.*[17] In general the

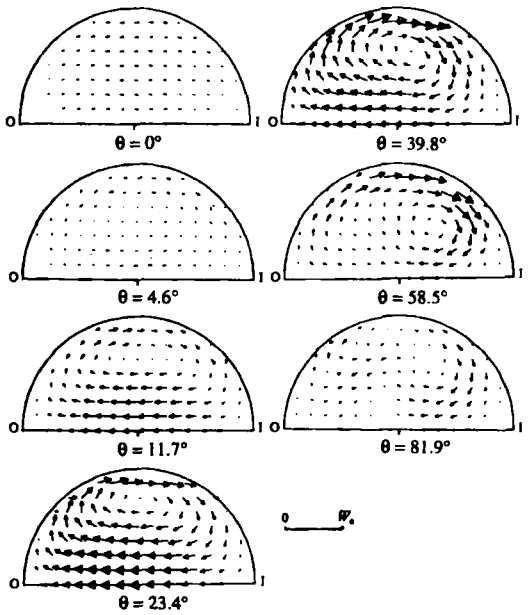

Figure 11(a). Development of secondary flow: experimental results obtained by Bovendeerd *et al.*[17] (O, outer bend; I, inner bend)

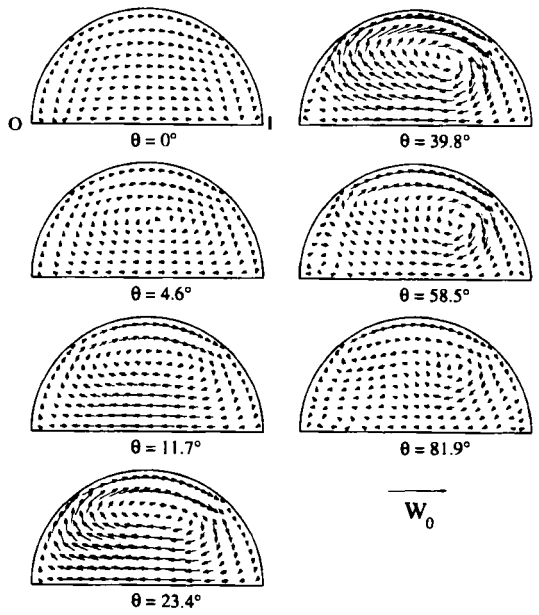

Figure 11(b). Development of secondary flow: predicted results (O, outer bend; I, inner bend)

development of the predicted secondary flow patterns as described above is quite similar to the experimental results shown in Figure 11(a).

Thermal stratification in a curved duct

Thermal stratification phenomena are experimentally investigated in a curved duct with two 90° curved parts as illustrated in Figure 12. Figure 12 also indicates sections A, B and C where the predicted vertical temperature distributions will be compared with experimental results. In the experiments a fluid of high temperature T_H is first supplied to the duct at constant flow rate so that the steady condition is established. After creating the steady state, the incoming fluid temperature is lowered to T_C, where the temperature difference $T_H - T_C$ is 10 K. The average

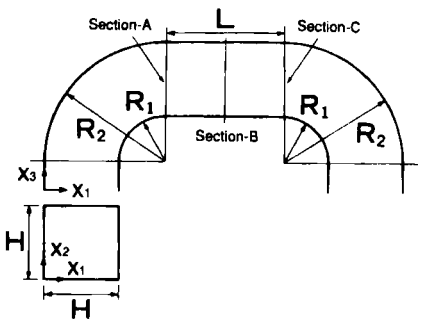

Figure 12. Geometry of curved duct (H = 50 mm; L = 80 mm; R_1 = 30 mm; R_2 = 80 mm, section B is located in middle of horizontal part)

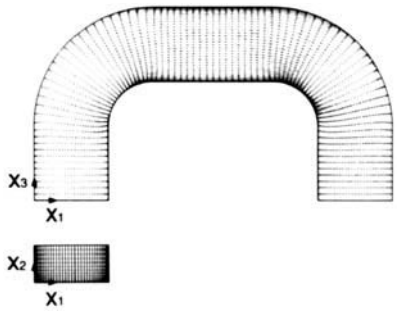

Figure 13. Grid distribution for curved duct

velocity in the duct, U_0, is maintained at about 10 mm s^{-1} throughout the steady and thermal transient conditions. The Reynolds and Richardson numbers are derived respectively as

$$Re = U_0 H/\nu_S = 500, \tag{21}$$

$$Ri = \beta g(T_H - T_C)H/U_0^2 = 9{\cdot}8. \tag{22}$$

Since the Richardson number is relatively high in this condition, the buoyancy force strongly affects the flow and the thermally stratified flow appears in the horizontal part of the duct.

Figure 13 shows the distribution of the computational grids generated by solving equation (2). Taking account of the symmetry in the transverse direction, the calculation area is set up from $x_2 = 0$ to 25 mm. The grid intervals are arranged to become finer in the vicinity of the solid walls with the aid of the control functions included in equation (2). The total grid number is $\xi_1 \times \xi_2 \times \xi_3 = 33 \times 13 \times 83 = 35{,}607$ and the number of grids where pressure is defined is $18 \times 8 \times 43 = 6192$.

Figure 14 shows the calculated flow pattern on the symmetrical vertical section in the steady state. Using this result as the initial condition at $t = 0$, the numerical analysis in the thermally transient condition proceeds; the fluid temperature at the inlet is lowered linearly by 10 K during 30 s, which approximately simulates the experimental condition, and the subsequent features are predicted until $t = 120$ s. Figure 15 shows the development of thermal stratification on the vertical section at $x_2 = 25$ mm. Since the contour maps for the experimental results indicated in Figure 15 were drawn from the measured values with 38 thermocouples, some isothermal lines lose their smoothness. In Figure 15 the normalized temperature is defined as $T^* = (T - T_C)/(T_H - T_C)$ and the interval of the isothermal lines is 0·1. The stratified thermal interface tends to decline towards the downstream direction in the horizontal area of the duct. As a result, higher-temperature fluid remains in the upper right corner of the curved area. As indicated in

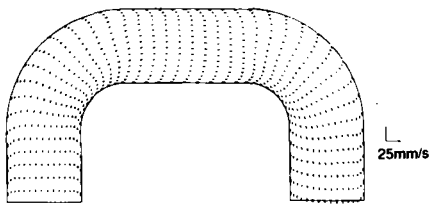

Figure 14. Calculated velocity vectors in steady state ($t = 0$)

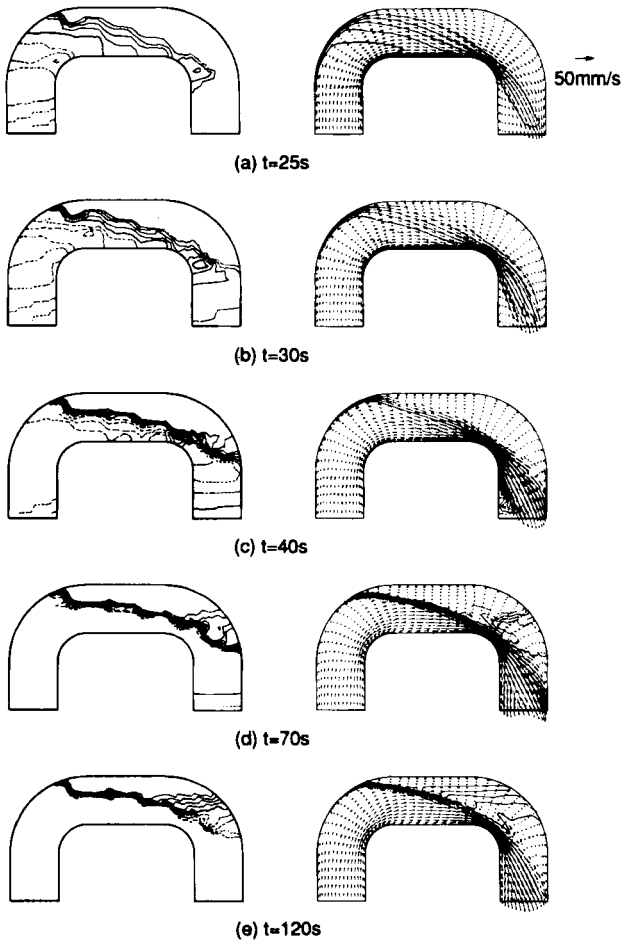

Figure 15. Comparison between experiments and calculated results (left, experimentally obtained isothermal lines; right, predicted velocity vectors and isothermal lines; thick lines, $T^* = 0{\cdot}5$; broken lines, $T^* = 0{\cdot}1$–$0{\cdot}4$)

the predicted result at $t = 40$ s, a weak counterclockwise vortex appears in the higher-temperature region and the cold fluid on the downstream side gradually rises up following the circulation. At $t = 120$ s the horizontally stratified region develops above the declined main stream. These numerically predicted features agree well with the experimental results. Figure 16 indicates the results of flow visualization by injecting fluorescent sodium into the cold fluid. It can be seen that the predicted progress of the thermal stratification also agrees well with these visualized results.

Figure 17 shows the flow patterns and isothermal lines on the vertical x_2–x_3 plane, sections A, B and C, as indicated in Figure 12. Figure 17(a) shows the results in the initial condition, in which different secondary flow patterns appear according to the sections. After $t = 25$ s, descending flows appear below the stratified thermal interface on sections B and C.

Figure 18 shows the vertical temperature distributions at $t = 120$ s on sections A, B and C; z indicates the vertical distance from the bottom surface of the horizontal part of a curved duct. In Figure 18 the thermal interface becomes lower in the order A, B, C as observed in

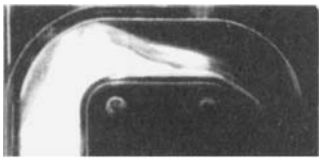

(a) t=25s

(b) t=30s

(c) t=40s

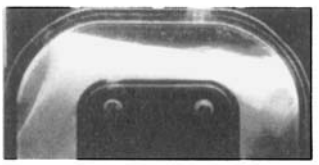

(d) t=70s

(e) t=120s

Figure 16. Visualized thermal stratification phenomena in experiments

Figure 15. While the numerically predicted thermal interface on section A is located slightly higher than that of the experimental result, it can be seen in general that the temperature distributions are satisfactorily simulated with the present numerical method.

4. CONCLUDING REMARKS

A numerical simulation method based on three-dimensional body-fitted co-ordinates has been developed in order to predict the buoyancy-influenced flows surrounded by arbitrarily shaped boundaries.

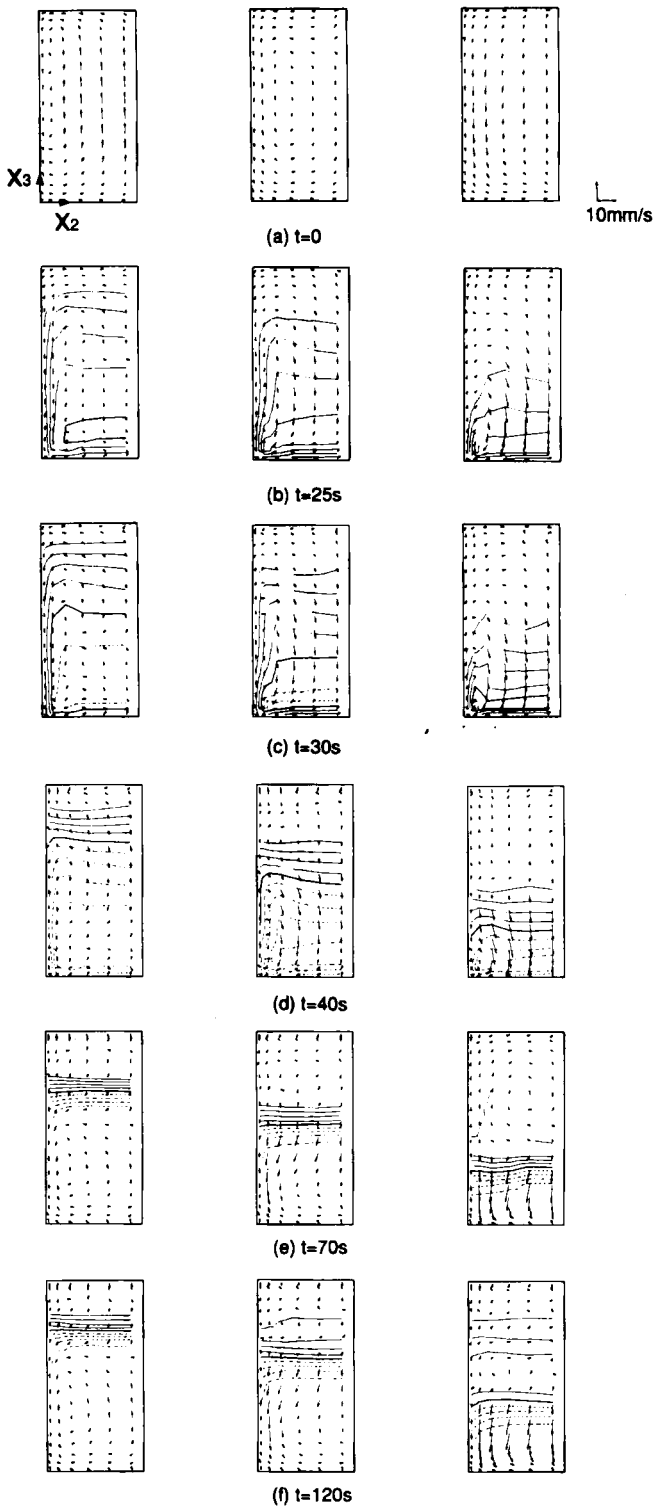

Figure 17. Predicted secondary flow and isothermal lines (left, section A; middle, section B; right, section C)

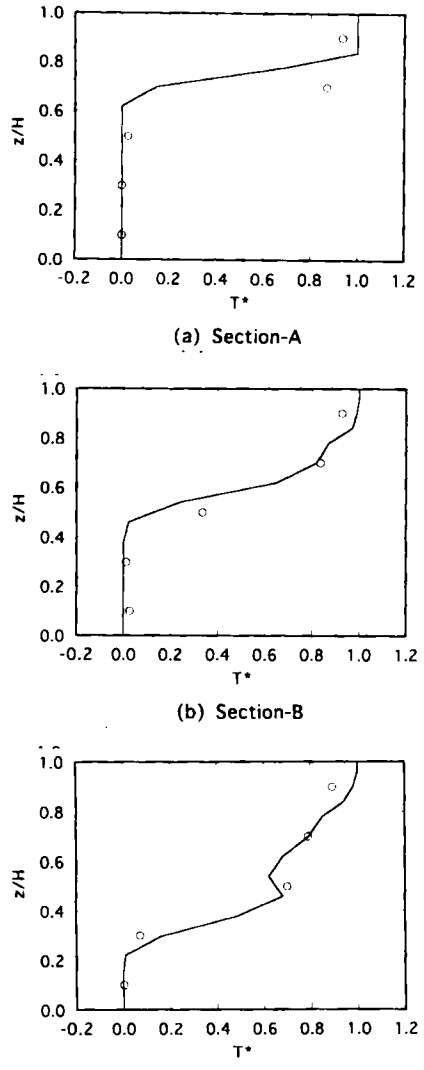

Figure 18. Vertical temperature distribution (t = 120 s; ○, experiment; —, calculation)

The curvilinear co-ordinate system is generated with the aid of GCSI, in which all variables in the computational domain are referred to derive cubic spline functions, and the metric coefficients are evaluated with less truncation error than by the usual methods. The numerical analyses of the transformed governing equations are based on a Lagrangian method. The convection terms are solved with LCSI, which enables us to obtain more accurate results than third-order polynomial interpolation or third-order upwind difference within a reasonable computational time. The buoyancy and diffusion terms are discretized in the Lagrangian schemes so as to have second-order accuracy with respect to time and space. In addition, the first and second derivatives included in these terms are obtained by making use of GCSI rather than the central difference method.

With regard to the boundary conditions, the Neumann conditions, which have been rather difficult for non-orthogonal curvilinear co-ordinates to deal with, are also able to be implemented with second-order accuracy in the present numerical method.

The developed prediction method was applied to a steady isothermal flow in a pipe with a 90° bend and to a thermally stratified flow in a curved duct. In the predicted results for the pipe flow the development of the secondary flow pattern as well as the axial velocity distribution have been reasonably simulated. In addition, regarding the stratified flow in a curved duct, some experimentally observed features, such as the declined shape of the thermal interface, the progress of thermal stratification and vertical temperature distributions in the horizontal part of the duct, have been satisfactorily predicted.

ACKNOWLEDGEMENTS

The author wishes to thank H. Karube and Mrs. Y. Nakazono for their contribution to this work.

APPENDIX: NOMENCLATURE

F_i external force in x_i-direction
g gravitational force
t time
T temperature
T_C lower temperature in transient condition
T_H higher temperature in transient condition
T_S standard temperature
u_i velocity component in x_i-direction
U_m contravariant velocity component
W_0 mean axial entrance velocity[17]

Greek letters

α thermal diffusivity
Δ thermal expansion coefficient
Δt time increment of the computation
$\Delta\rho$ $\rho - \rho_S$
ν_S kinematic viscosity at $T = T_S$
ρ fluid density
ρ_S fluid density at $T = T_S$

REFERENCES

1. J. F. Thompson, Z. U. A. Warsi and C. W. Mastin, *Numerical Grid Generation*, Elsevier, New York, 1985.
2. A. J. Winslow, 'Numerical solution of the quasi-linear Poisson equation in a non-uniform triangular mesh', *J. Comput. Phys.*, **2**, 149 (1966).
3. W. D. Barfield, 'An optimal mesh generator for Lagrangian hydrodynamic calculations in two space dimensions', *J. Comput. Phys.*, **6**, 417 (1970).
4. W. H. Chu, 'Development of a general finite difference approximation for a general domain, Part I, Machine transformation', *J. Comput. Phys.*, **8**, 392 (1971).
5. A. A. Amsden and C. W. Hirt, 'A simple scheme for generating general curvilinear grids', *J. Comput. Phys.*, **11**, 348 (1973).

6. J. F. Thompson, F. C. Thames and C. W. Mastin, 'Automatic numerical generation of body-fitted curvilinear coordinate system for field containing any number of arbitrary two-dimensional bodies', *J. Comput. Phys.*, **15**, 299–319 (1974).
7. J. F. Thompson, F. C. Thames and C. W. Mastin, 'Body-fitted curvilinear coordinate system for solution of partial differential equations on fields containing any number of arbitrary two-dimensional bodies', *NASA CR-2729*, 1976.
8. J. F. Thompson, F. C. Thames and C. W. Mastin, 'TOMCAT—a code for numerical generation of boundary-fitted curvilinear coordinate systems on fields containing any number of arbitrary two-dimensional bodies', *J. Comput. Phys.*, **24**, 274–302 (1977).
9. K. Hsu and S. L. Lee, 'A numerical technique for two-dimensional grid generation with grid control at all of the boundaries', *J. Comput. Phys.*, **96**, 451–469 (1991).
10. J. F. Thompson, Z. U. A. Warsi and B. B. Amlicke, 'Numerical solutions for laminar and turbulent viscous flow over single and multi-element airfoils using body-fitted coordinate system', *NASA CP-2001*, 1976.
11. F. C. Thames, J. F. Thompson and C W. Mastin, 'Numerical solutions for viscous and potential flow about arbitrary two-dimensional bodies using body-fitted coordinate system', *J. Comput. Phys.*, **24**, 245–273 (1977).
12. J. L. Steger, 'Implicit finite-difference stimulation of flow about arbitrary two-dimensional geometries', *AIAA J.*, **16**, 679–686 (1978).
13. S. Ogawa and T. Ishiguro, 'A method for computing flow fields around moving bodies', *J. Comput. Phys.*, **69**, 49–68 (1987).
14. T. Kawamura and K. Kuwahara, 'Computation of high Reynolds number flow around a circular cylinder with surface roughness', *AIAA-84-0304*, 1984.
15. F. M. Holly Jr. and A. Preissmann, 'Accurate calculation of transport in two dimensions', *J. Hydraul. Div., ASCE*, **103**, 1259–1277 (1977).
16. G. A. Schohl and F. M. Holly Jr., 'Cubic-spline interpolation in Lagrangian advection computation', *J. Hydraul. Eng., ASCE*, **117**, 248–253 (1991).
17. P. H. M. Bovendeerd, A. A. Van Steenhoven, F. N. Van de Vosse and G. Vossers, 'Steady entry flow in a curved pipe', *J. Fluid Mech.*, **177**, 233–246 (1987).
18. D. K. Lilly, 'On the computational stability of numerical solutions of time-dependent nonlinear geophysical fluid dynamics problem', *U.S. Weather Bur. Mon. Weather Rev.*, **93**, 11–26 (1965).
19. F. H. Harlow and J. E. Welch, 'Numerical calculation of time-dependent viscous incompressible flow of fluid with free surface', *Phys. Fluids*, **8**, 2182—2189 (1965).
20. S. Ushijima, S. Moriya and N. Tanaka, 'Internal standing waves in a cylindrical vessel and their near-wall features', *ASME, J. Heat Transfer*, **115**, 613–620 (1993).
21. M. Chapman, 'FRAM—nonlinear damping algorithms for the continuity equation', *J. Comput. Phys.*, **44**, 84–103 (1981).